A Transient URANS Workflow for Stability-Derivative Estimation of a Fixed-Wing sUAS Including External Payload and Landing Gear Aerodynamics

Harsh Gupta[1]
University of Georga, Athens, Georgia, 30601, United States

This work establishes the underpinning for estimating aerodynamic stability derivatives of a fixed-wing small unmanned aerial system (sUAS) using Unsteady Reynolds-Averaged Navier–Stokes (URANS) simulations. While vortex lattice methods (VLM) are widely used for preliminary stability prediction in low-Reynolds-number flight regimes, they neglect viscous and separated flow effects that become significant in the presence of unconventional fuselage geometries, externally mounted payloads, and fixed landing gear. Finite-difference perturbations in angle of attack were applied within steady RANS simulations to extract pitching moment derivatives. The resulting moment histories exhibited persistent oscillations, indicating vortex shedding and unsteady wake interactions not captured by steady-state assumptions. This observation motivates the use of URANS to resolve time-dependent flow structures influencing stability behavior. Results demonstrate that VLM overpredicts longitudinal static stability for the low-Reynolds-number sUAS configuration considered, with CFD-based derivatives yielding approximately 50% lower restorative pitching moment magnitude. These findings highlight the importance of unsteady viscous modeling for accurately predicting stability characteristics of complex sUAS geometries.

I. Introduction

Accurate estimation of aerodynamic stability derivatives is essential for the design of passively stable small unmanned aerial systems (sUAS), particularly in low-Reynolds-number flight regimes where viscous and separated flow effects become significant. Longitudinal static stability, commonly characterized by the pitching moment derivative with respect to angle of attack, $C_{M\alpha}$, governs the aircraft's ability to restore equilibrium following a disturbance. For configurations that rely solely on passive stability – without active control augmentation – precise prediction of this derivative is critical during early-stage design. Lightweight vortex lattice methods (VLM), including tools such as AVL and XFLR5, are widely used for preliminary aerodynamic modeling due to their computational efficiency. However, these inviscid formulations neglect viscous wake dynamics and cannot fully capture the aerodynamic influence of bluff fuselages, static landing gear, and externally mounted payloads. In mission-optimized sUAS configurations, where packaging constraints often lead to unconventional outer-mold-line geometries, these non-lifting components may significantly influence the overall pitching moment behavior.

To investigate these effects, steady Reynolds-Averaged Navier–Stokes (RANS) simulations were conducted for a fixed-wing sUAS configuration representative of a low-Reynolds-number design. Finite-difference perturbations in angle of attack were applied to extract $C_{M\alpha}$ from computed pitching moments. While residual convergence criteria were satisfied, the resulting moment histories exhibited persistent oscillatory behavior. Flow visualization revealed vortex shedding and unsteady wake interactions originating from external geometries, indicating that time-dependent flow structures contribute to the measured aerodynamic moments. These observations suggest that steady-state RANS

[1] Student, UGA College of Engineering, AIAA Student Member

assumptions may be insufficient for accurately evaluating stability derivatives in such configurations. The presence of unsteady vortex dynamics motivates the use of Unsteady RANS (URANS) formulations to resolve transient flow structures and obtain time-averaged stability derivatives. This study therefore evaluates the discrepancies between vortex lattice predictions and viscous CFD-derived derivatives, and establishes a computational basis for justifying URANS-based stability analysis in future work.

II. Background

A. Aircraft Overview

The aircraft configuration analyzed in this study was generated using a multidisciplinary design optimization (MDO) framework developed in MATLAB to maximize mission performance for the 2025–2026 AIAA Design–Build–Fly competition. The optimization process, summarized in Fig. 1, evaluates mission score through a physics-based mission simulator that models aerodynamic performance, propulsion efficiency, structural mass, and energy consumption. More than 3 million parameter combinations were evaluated to determine an optimal configuration.

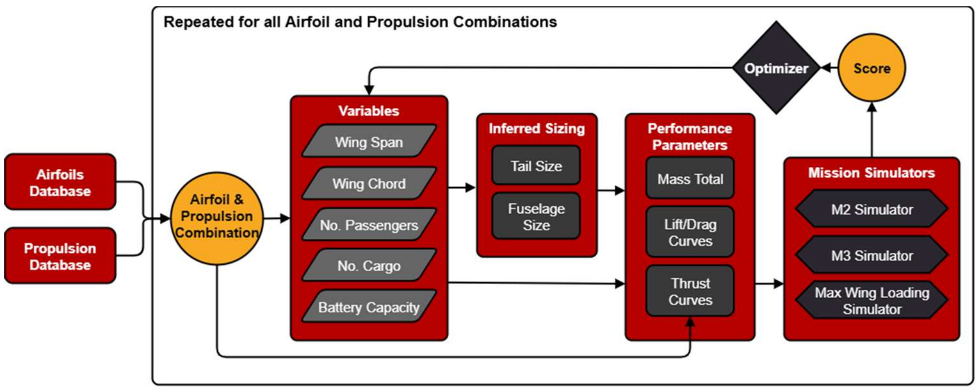

Fig. 1 Aircraft optimizing framework overview.

The optimization variables considered included main-wing airfoil selection, wingspan, chord, propulsion system (motor and propeller), payload capacity, and onboard energy storage. A particle swarm optimization (PSO) algorithm was used to navigate the design space and maximize mission score. The resulting configuration features a relatively bluff fuselage and high payload density driven by mission requirements, producing a geometry that deviates from conventional slender-body aircraft assumptions typically used in preliminary stability analysis.

Following wing and propulsion optimization, the next stage of aerodynamic development is tail sizing to satisfy longitudinal and directional static stability requirements. The horizontal and vertical stabilizer span and chord must be selected to produce adequate stability derivatives for a configuration characterized by: Eppler E748 main wing airfoil, 1.500m wingspan, 0.269 m wing chord, and shaped payload integration within a compact fuselage volume.

Structural constraints further restrict tail airfoil selection. To accommodate required spar dimensions, the stabilizer airfoils must have a minimum thickness-to-chord ratio of 12%. To minimize additional drag while satisfying this constraint, a symmetric NACA 0012 airfoil was selected for both horizontal and vertical tail surfaces. The symmetric profile eliminates baseline camber-induced pitching moment contributions from the tail and simplifies interpretation of the computed stability derivatives.

The mission-driven outer-mold-line geometry, including the bluff fuselage and external components, introduces flow separation and wake interactions that are not fully captured by inviscid vortex lattice methods. Consequently, this configuration provides a suitable test case for evaluating the limitations of steady RANS in extracting accurate longitudinal stability derivatives.

B. System Figure

The three-dimensional aircraft geometry was modeled in Onshape using the optimized wing and fuselage parameters described previously. Fig. 2 shows the top and side planform views of the configuration. The fuselage width is explicitly illustrated, as it significantly influences the effective aspect ratio of the main wing and modifies the aerodynamic center location relative to conventional slender-body assumptions. The fuselage geometry was designed to accommodate the mission-optimized payload configuration (40 rubber ducks and 13 hockey pucks) and was provided by the structural design team. Manufacturing tolerances were incorporated into the final wingspan and chord to account for balsa wood and carbon fiber composite construction methods.

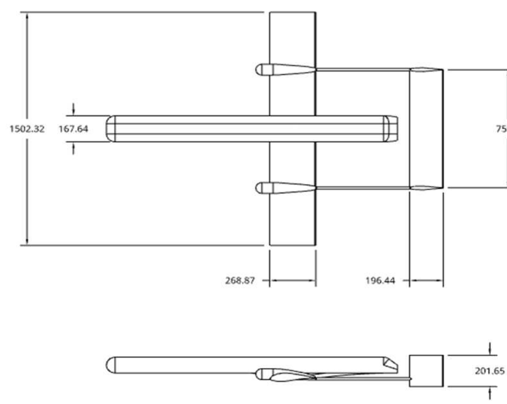

Fig. 2 Top and side view of Archangel planform (mm).

Following wing and propulsion optimization, preliminary tail sizing was performed using the tail volume coefficient (TVC) method, a classical stability-based approach widely applied in preliminary aircraft design [1]. The method determines required horizontal and vertical stabilizer planform areas using empirically derived volume coefficients based on historical aircraft data. The governing relations are given in Eq. (1) and Eq. (2).

$$V_h = \frac{S_{HT} L_H}{S_W \bar{c}} \tag{1}$$

$$V_v = \frac{S_{VT} L_V}{S_W b} \tag{2}$$

S_{HT} and S_{VT} are the horizontal and vertical tail 2D planform areas, S_W is the main wing planform area, $\bar{c}$ is the main wing mean geometric chord, b is the main wing span, and L_H and L_V are the horizontal and vertical tail moment arms. Volume coefficients V_h and V_v were selected based on historical data for multi-engine turboprop cargo aircraft with relatively large fuselage volumes and stable cruise characteristics. These aircraft provided the closest geometric and mission similarity to the present configuration. Using this method, the preliminary tail geometry was determined to be $S_{HT} = 0.154$ m_2 and $S_{VT} = 0.061$ m_2 along with a tail moment arm of $L_H = L_v = 0.796$ m. The decomposition of these specifications into tail geometry is shown in Fig 2.

C. Benchmarking

Pitching moment derivatives from prior Design–Build–Fly (DBF) aircraft were reviewed to establish expected magnitudes for longitudinal static stability. Final reports from leading teams in the 2018, 2022, and 2024 competitions were analyzed to extract representative values of $C_{M\alpha}$. The 2022 FH Joanneum aircraft reported C_{M_α} = -0.018 1/deg obtained from a linear fit of pitching moment coefficient versus angle of attack computed from AVL [2]. The 2024 USC configuration reported C_{M_α} = -0.011 1/deg computed from AVL [3]. Georgia Tech's 2018 wind tunnel results yielded C_{M_α} = -0.006 1/deg demonstrating a weaker stability response relative to corresponding their vortex lattice predictions using VORLAX, another VLM solver similar to AVL and XFLR5 [4].

Across these studies, vortex lattice solvers, including AVL and XFLR5, consistently predicted larger-magnitude pitching moment derivatives than those obtained experimentally or through higher-fidelity analysis. This trend has been attributed to inviscid modeling assumptions and simplified wake representations inherent in vortex lattice methods. XFLR5 documentation similarly notes a tendency to overpredict longitudinal stability derivatives.

From this benchmarking analysis, it is reasonable to expect $C_{M_\alpha}$to be negative and on the order of 10^{-2} 1/deg for passively stable DBF-scale aircraft. Additionally, vortex lattice predictions are anticipated to yield larger-magnitude derivatives than viscous CFD-based estimates, motivating direct comparison between the two approaches in this study.

III. CFD Analysis

A. Governing Equations and Solver Model

The aerodynamic simulations were performed using the Reynolds-Averaged Navier–Stokes (RANS) equations for incompressible flow. The governing equations consist of the time-averaged continuity and momentum equations Eq. 3 and Eq. 4, where the Reynolds stress term $\overline{\mathbf{u}'\mathbf{u}'}$ is modeled using a two-equation turbulence closure.

$$\nabla \cdot \mathbf{u} = 0 \tag{3}$$

$$\rho(\mathbf{u} \cdot \nabla)\mathbf{u} = -\nabla p + \mu \nabla^2 \mathbf{u} - \nabla \cdot \overline{\mathbf{u}'\mathbf{u}'} \tag{4}$$

Turbulence effects were modeled using the k–ω Shear Stress Transport (SST) formulation. This model blends the near-wall accuracy of the k–ω model with the free-stream robustness of the k–ε model through a smooth blending function. The k–ω SST model was selected due to the moderate Reynolds number regime of the present configuration (Re ≈ 4.75×10^5 to 6.5×10^5), where transitional effects and near-wall modeling accuracy are critical. Prior studies have shown improved boundary layer and separation prediction using SST in low-Re external aerodynamic flows [5].
The following modeling assumptions were applied:

1) Incompressible flow: Density was treated as constant, appropriate for low-speed flight conditions.
2) Steady RANS formulation: Time-averaged equations were solved; transient fluctuations were not explicitly resolved.
3) Constant fluid properties: Air viscosity and density were held constant at standard atmospheric conditions.
4) Three-dimensional viscous flow: All velocity components were retained; viscous effects were modeled explicitly.
5) Turbulence modeling via k–ω SST: Both laminar and turbulent regions were captured through transport equations for turbulent kinetic energy k and specific dissipation rate ω.
6) No energy equation: Thermal effects were neglected due to the absence of significant compressibility or heat transfer.

B. Mesh Definition

To evaluate the prototype tail geometry, a far-field enclosure was generated around the aircraft and meshed for analysis in ANSYS Fluent. The Onshape CAD geometry was repaired in SpaceClaim and imported into ANSYS Discovery to generate the computational enclosure and define appropriate named selections.

A primary box enclosure extending 200% beyond the aircraft in the x, y, and z directions was constructed to minimize boundary interference effects. A secondary spherical enclosure with a 25% extension relative to the primary domain was centered at the aircraft centroid to act as a body of influence for localized mesh refinement. An XZ symmetry plane was applied to reduce computational cost, consistent with the specified boundary conditions. Only the two enclosures were retained for the final mesh generation.

To resolve viscous effects within the Reynolds number range of 450,000 to 650,000, boundary layer inflation was applied. The first layer height was determined based on a target $Y^+ = 50$ [6]. Using laminar flat-plate correlations, the first layer height was calculated to be 9.43×10^{-5}m. This places the first inflation layer within the logarithmic region of the near-wall boundary layer [6], enabling appropriate near-wall modeling. While wall-function treatment is not strictly required for the k–ω SST formulation, reduced first-layer height improves near-wall resolution and overall model fidelity [5]. Close-up views of the inflation layers are shown in Fig. 3 and Fig. 4.

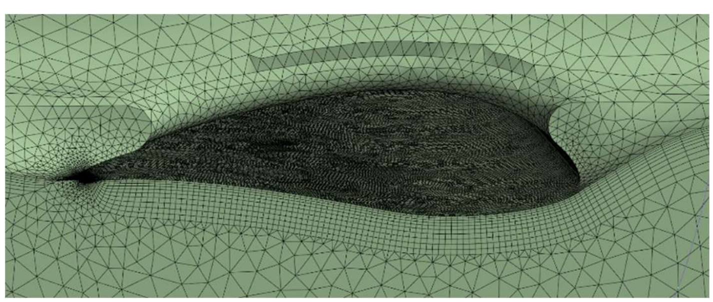

Fig. 3 Inflation close-up around the main wing

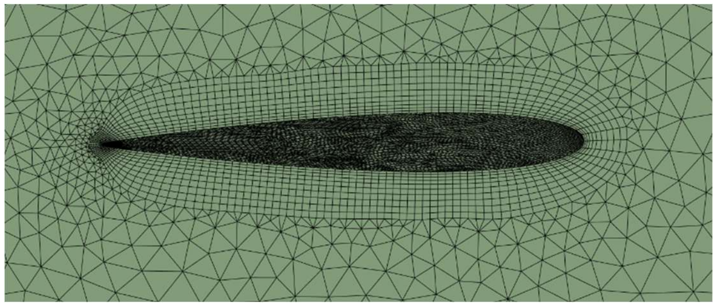

Fig. 4 Inflation close-up around horizontal stabilizer

Additional surface and edge refinement was applied to improve geometric resolution of critical aerodynamic features. Mesh sizing was reduced along the airfoil surfaces and trailing edges of the main wing and tail stabilizers, as well as around the cylindrical boom connecting the wing to the tail assembly, as shown in Fig 5. Local element sizes were specified as follows: 0.001 m at trailing edges, 0.0075 m along airfoil faces, and 0.002 m around the cylindrical boom. A close-up of the refined mesh is shown in Fig. 5.

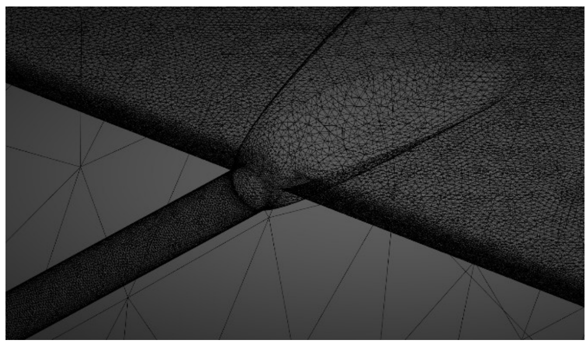

Fig. 5 Close-up wireframe view of the main wing trailing edge

The cell count for the final mesh was roughly 4.5 million, with a significant portion of these accounted by the wedge cells found in inflation layers around the aircraft. Mesh metrics were generated, and the quality of the worst elements is shown in Fig. 6. The skewness and orthogonal quality for most cells was deemed to be acceptable.

Sheet | Solid | Solid - Surface

Quality Criterion	Warning Limit	Error (Failure) Limit	Worst
Max Aspect Ratio	Default (5)	Default (1000)	51.37
Min Element Quality	Default (0.05)	Default (5e-04)	0.025
Min Orthogonal Quality	Default (0.05)	Default (5e-03)	0.094
Max Skewness	Default (0.9)	Default (0.999)	0.9

Fig. 6 Mesh quality worksheet

C. Solution Procedure and Stability Derivative Extraction

Following mesh generation, steady RANS simulations were conducted in ANSYS Fluent using the boundary conditions and turbulence model described previously. Two angles of attack were evaluated: $\alpha = 0°$ and $\alpha = -1°$. These operating points were selected to compute the longitudinal static stability derivative using a finite-difference approximation. Residual histories for both simulations exhibited nearly identical convergence behavior. The residual report for the 0°case is shown in Fig. 7. Convergence was achieved with continuity residuals below 1×10^{-3}, turbulence residuals (k and ω) on the order of 5×10^{-5}, and velocity residuals in the x–y directions on the order of 5×10^{-8}. These values indicate acceptable steady-state convergence for external aerodynamic analysis.

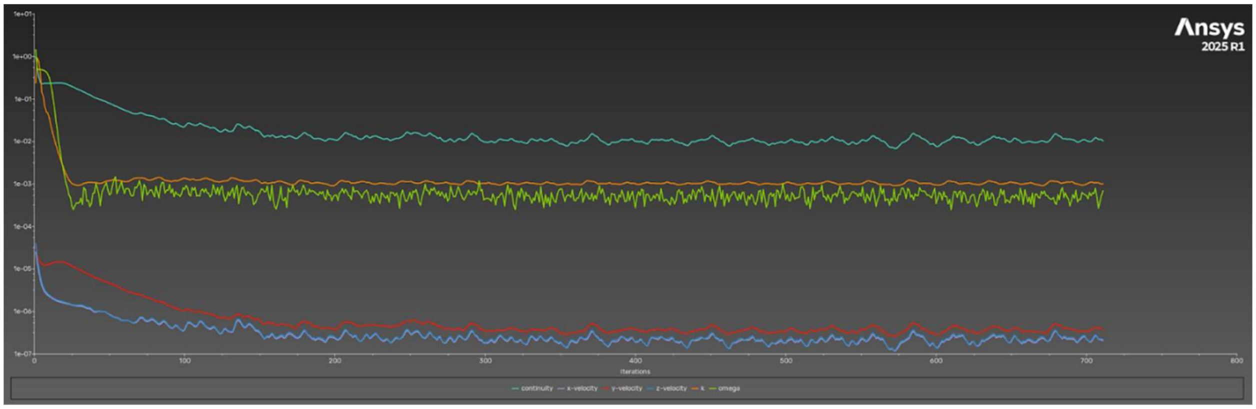

Fig. 7 Residual report from 0 deg angle of attack simulation

Moment reports were generated about the defined reference origin (see prototype development section). Despite residual convergence, the pitching moment histories exhibited persistent oscillations, characteristic of separated external flow and vortex shedding behavior. These fluctuations are shown in Fig 8 and Fig 9. To obtain representative steady values, the pitching moment was averaged over the final 400 iterations of each simulation.

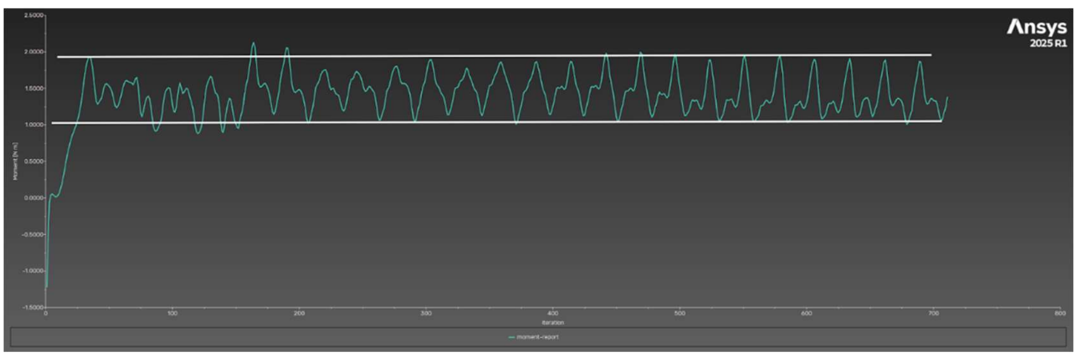

Fig. 8 Moment report for 0 deg angle of attack simulation

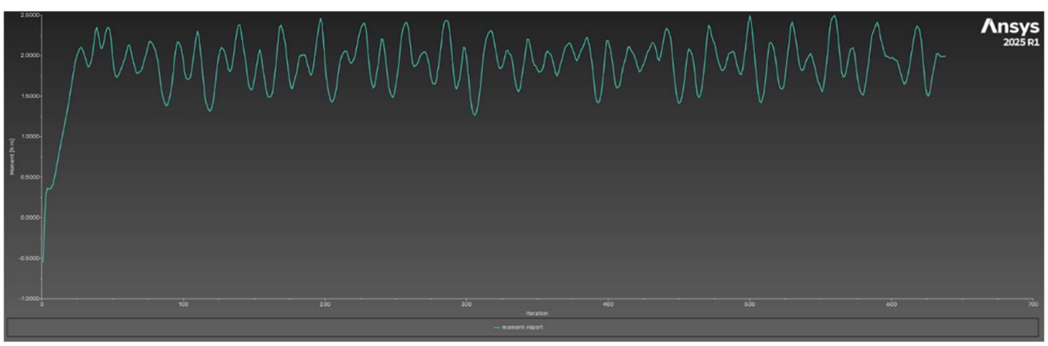

Fig 9. Moment report for -1 deg angle of attack simulation

Accounting for symmetry boundary conditions, which required all forces acting on the aircraft to be doubled in post processing, the following moments were determined:

- At 0 deg angle of attack: M = 3.046 Nm
- At -1 deg angle of attack: M = 3.930 Nm

The pitching moment coefficient was computed using Eq. 5. where $q = \frac{1}{2}\rho V^2$ is dynamic pressure, $S = 0.403\ \mathrm{m}^2$ is the wing reference area, and $c = 0.269$ m is the reference chord.

$$C_M = \frac{M}{qSc} \tag{5}$$

The resulting coefficients were:

- At 0 deg angle of attack: $C_M = 0.0733$
- At -1 deg angle of attack: $C_M = 0.09458$

The longitudinal static stability derivative was computed using a linear finite-difference approximation:

$$C_{M_\alpha} \approx \frac{C_{M,0^\circ} - C_{M,-1^\circ}}{0-(-1)} \tag{6}$$

$$C_{M_\alpha} = -0.02127 \text{ deg}^{-1}$$

D. Flow Visualization

Velocity pathlines were generated to examine wake development and separated flow structures downstream of the fuselage and wing. These visualizations provide insight into the physical mechanisms contributing to the reduced longitudinal stability derivative observed in the CFD results. As shown in Fig. 10, the fuselage generates a substantial wake that continues downstream and envelops a significant portion of the horizontal stabilizer.

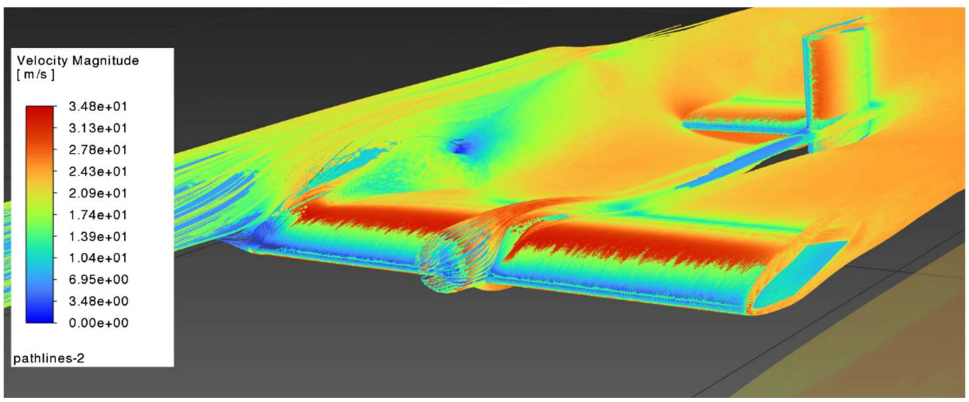

Fig. 10 Velocity pathlines released from aircraft skin

This wake interaction reduces the effective dynamic pressure and local angle of attack experienced by the horizontal tail, thereby diminishing its lift contribution. Because the horizontal stabilizer provides the primary restorative pitching moment for longitudinal stability, this wake shielding effect reduces the magnitude of C_{M_α}relative to predictions from inviscid vortex lattice methods. In contrast, XFLR5 does not model viscous wake thickening or separated flow structures generated by bluff fuselage geometries. As a result, the horizontal stabilizer in the vortex lattice solution experiences nearly freestream conditions, leading to an overprediction of tail effectiveness and consequently a larger-magnitude pitching moment derivative.

IV. VLM Analysis using XFLR5

The longitudinal stability derivative was independently evaluated using the XFLR5 vortex lattice solver. XFLR5 models three-dimensional lifting surfaces using a discretized vortex lattice representation, where bound vortices are distributed over the wing and tail planforms. Aerodynamic forces are computed by enforcing flow tangency conditions on each panel, while sectional lift and drag data are obtained from two-dimensional viscous airfoil analyses.
The aircraft geometry was reconstructed in XFLR5 as shown in Fig. 11.

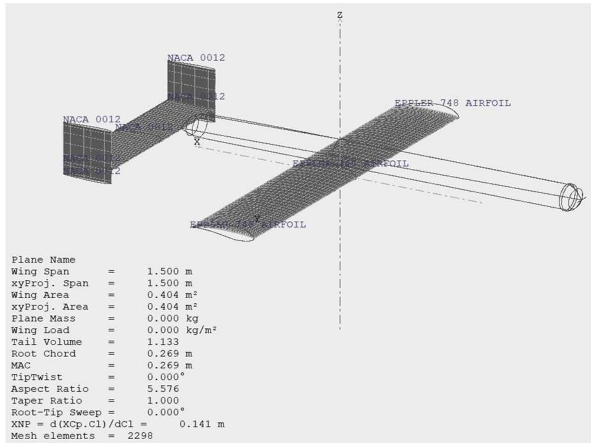

Fig. 11 Aircraft model in XFLR5

Pitching moment coefficients were computed over an angle-of-attack range from −10° to 25°. Linear regression of the C_M–α curve yielded:

- $C_{M0} = 0.069$
- $C_{M_\alpha} = -0.045\ \text{deg}^{-1}$

The value of C_{M0} compares closely with the steady RANS result, exhibiting a percent difference of 5.63%. However, the predicted stability derivative differed significantly, with XFLR5 yielding a 71.67% larger magnitude for C_{M_α} relative to the CFD-derived value.

This trend is consistent with prior benchmarking studies, including Georgia Tech's 2018 report, which observed that vortex lattice methods tend to overpredict longitudinal stability derivatives. The discrepancy arises from fundamental modeling assumptions: vortex lattice solvers neglect viscous wake thickening, separation, and fuselage–tail wake interaction effects [7,8]. As a result, the horizontal stabilizer is assumed to operate in near-freestream conditions, leading to an overestimation of tail lift effectiveness at nonzero angles of attack. In contrast, the RANS simulations capture wake shielding from the fuselage and separated flow structures, reducing the effective dynamic pressure at the tail and thereby decreasing the magnitude of the restorative pitching moment. Additionally, the vortex lattice formulation does not provide insight into unsteady flow behavior, including the oscillatory moment responses observed in the CFD analysis.

V. Conclusion

This study evaluated longitudinal static stability prediction for a low-Reynolds-number, mission-optimized fixed-wing sUAS configuration with a bluff fuselage. A baseline tail geometry was developed using the tail volume coefficient method, and the longitudinal static stability derivative C_{M_α} was extracted using finite-difference perturbations in angle of attack within steady RANS simulations. The CFD results produced a negative C_{M_α} with $C_{M_\alpha} = -0.02127\ \text{deg}^{-1}$, indicating static longitudinal stability for the analyzed cruise condition and supporting the adequacy of the preliminary tail sizing.

However, despite residual convergence, the steady RANS moment histories exhibited persistent oscillations, and flow visualization demonstrated wake shielding of the horizontal stabilizer by the fuselage. These results indicate that viscous wake interaction and separated flow structures materially reduce tail effectiveness and the resulting restorative pitching moment compared to inviscid assumptions. Consistent with both the DBF benchmarking review and prior literature trends, the XFLR5 vortex lattice model produced a comparable C_{M0} but substantially overpredicted the stability derivative magnitude, with $C_{M_\alpha} = -0.045\ \text{deg}^{-1}$ (71.67% larger magnitude than the CFD-derived value). Taken together, these findings show that vortex lattice methods may be insufficient for stability derivative evaluation when external geometries generate separation and unsteady wakes, and they suggest that steady RANS alone may not fully capture the time-dependent mechanisms contributing to the aircraft's aerodynamic moments.

The observed oscillatory pitching moment response is particularly relevant for passively stable DBF-scale aircraft, where unsteady flow can reduce effective stability margins and lead to marginal dynamic behavior even when static derivatives are nominally acceptable. As a result, the primary outcome of this work is a justified pathway toward URANS-based stability derivative evaluation for complex, low-Reynolds-number sUAS configurations. Future work will (i) perform URANS simulations to quantify time-averaged stability derivatives and characterize the frequency and amplitude content of moment fluctuations, and (ii) correlate these predictions with experimental data from the DBF aircraft to determine how the measured unsteadiness influences effective stability in flight. This combined computational and experimental approach is expected to improve stability modeling fidelity for unconventional sUAS geometries and provide actionable guidance for tail design refinement under low-Reynolds-number, wake-dominated operating conditions.

References

[1] Gudmundsson, S., *General Aviation Aircraft Design: Applied Methods and Procedures*, 2nd ed., Elsevier, Amsterdam, 2022.

[2] American Institute of Aeronautics and Astronautics, “2022 DBF Top 3 Reports,” AIAA, 2022. URL: https://aiaa.org/wp-content/uploads/2024/12/2022-aiaa-dbf-top-3-reportsd97c1337115848488c92228e188607c7.pdf

[3] American Institute of Aeronautics and Astronautics, “2024 DBF Top 3 Reports,” AIAA, 2024. URL: https://aiaa.org/wp-content/uploads/2024/12/2024-dbf-top-3-reports.pdf

[4] American Institute of Aeronautics and Astronautics, “Winning Reports – February 2018,” AIAA, 2018. URL: https://aiaa.org/wp-content/uploads/2024/12/winning-reports-feb-2018.pdf

[5] Tominaga, Y., “Unsteady Flow Fluctuation Behind the Bluff Body: Comparison with Experimental Results,” *Atmospheric Environment*, Vol. 114, 2015, pp. 27–37, doi: 10.1016/j.atmosenv.2015.05.012

[6] Versteeg, H. K., and Malalasekera, W., *An Introduction to Computational Fluid Dynamics: The Finite Volume Method*, 2nd ed., Pearson Education, Harlow, England, UK, 2007, Chap. 9.

[7] XFLR5 Development Team, “XFLR5 Results vs Prediction,” XFLR5 Documentation, 2024. URL: https://www.xflr5.tech/docs/Results_vs_Prediction.pdf

[8] XFLR5 Development Team, “XFLR5 Limitations,” XFLR5 Documentation, 2024. URL: https://www.xflr5.tech/docs/Part%20IV:%20Limitations.pdf